ELSEVIER

Contents lists available at ScienceDirect

International Journal of Mechanical Sciences

journal homepage: www.elsevier.com/locate/ijmecsci





Broadband unidirectional vibration transmissibility governed by an eigenfrequency-transmissibility correlation

Liling Tang a,b,†,**, Shuowei An c,†, Yuguang Chen a, Debin Li a, Li Cheng c,*,

- ^a School of Aeronautics and Astronautics, Shenzhen Campus, Sun Yat-Sen University, Shenzhen, China
- ^b State Key Laboratory for Strength and Vibration of Mechanical Structures, Xi'an, China
- ^c Department of Mechanical Engineering, The Hong Kong Polytechnic University, Hung Hom, Kowloon, Hong Kong, China

ARTICLE INFO

Keywords: Unidirectional transmission Asymmetric structures Wave propagation Unidirectional vibration transmissibility Periodic structures Eigenfrequency-transmissibility correlation

ABSTRACT

Unidirectional transmission is attracting increasing attention for applications in wave manipulation and sensing. Although asymmetric wave scattering in acousto-elastic systems is well-studied, asymmetric dynamic responses of finite structures remain less exploited and poorly understood, in terms of underlying mechanisms and design strategy. This work proposes a universal principle, referred to as eigenfrequency-transmissibility correlation, to elucidate how the unidirectional vibration transmissibility (UVT) would occur and behave in asymmetric finite structures. We analytically demonstrate such correlation through a simplified model to show that transmissibility extrema occur at the anti-resonance frequencies with vanishing response at excitation point, which strictly correspond to the eigenfrequencies of the adjoint subsystem or complementary subsystem with the excitation point fixed. Guided by this principle, a periodic beam with inherent asymmetry and broadband bandgap is designed, in which both theoretical and experimental results demonstrate a bilateral transmissibility difference exceeding 20 dB across a 4500 Hz bandwidth, testifying a broadband high-efficiency UVT. These findings provide a fundamental understanding on asymmetric dynamics and a generalized design framework for high-performance unidirectional wave devices.

1. Introduction

Unidirectional transmission (UT), which refers to the phenomenon of one-way wave scattering or asymmetric dynamic response, has garnered increasing attention owing to its wide applications in wave manipulation, sensing, imaging, and communications. UT is typically achieved by introducing nonlinearities into systems [1], such as strongly nonlinear material [2,3], nonlinear circuits [4], nonlinear springs [5–7], and nonlinear Hertz contact force [8], etc. Other approaches to achieve UT consist in breaking the time-reversal symmetry by utilizing additional perturbation [9], magnetic field [10], flow field [11–14] or spatiotemporal modulation [15–18]. By adding the ingredients such as band topology [19–21] and non-Hermiticity [22,23], robust and nonreciprocal wave propagation can be achieved as well. Though effective for the attainment of non-reciprocity, these approaches face limitations in practical implementation especially in terms of nonlinearity control and massive external energy or field modulation.

A promising alternative strategy involves breaking structural symmetry exclusively through linear designs to achieve reciprocal UT. Asymmetric wave scattering has been widely investigated in both acoustic and elastic wave systems. Examples include gradient structures with asymmetric refraction [24-27] or diffraction [28-31], mode-converted superlattices [32-36], topological insulators with localized states [37-40], non-Hermitian systems with exceptional points [41-43], as well as directional waveguide through partial bandgaps of PCs [44-48]. As for the dynamic response of relevant finite structures, the above scattering analysis may apply to certain extent when the effects of boundary conditions are insignificant, such as expected non-trivial localized states in most finite topological insulators according to the principle of bulk-boundary correspondence [49-51]. However, in most cases, the dynamic response of finite structures significantly differs from the predictions based solely on wave propagation in infinite media, exemplified by the resonances within bandgap regions induced by the boundary truncations [52-57]. Studies of wave

^{*} Corresponding author.

^{**} Corresponding author at: School of Aeronautics and Astronautics, Shenzhen Campus, Sun Yat-Sen University, Shenzhen, China. *E-mail addresses*: tanglling@sysu.edu.cn (L. Tang), li.cheng@polyu.edu.hk (L. Cheng).

[†] These two authors contribute equally.

Fig. 1. (a) A general n-dimensional spring-mass system: its (i-1)-dimensional subsystem and (n-i)-dimensional complementary subsystem with fixed m_{ij} (b) a periodic spring-mass system.

scatterings in infinite systems cannot be directly applied to finite systems.

Unfortunately, existing works on asymmetric dynamic responses in finite systems remain limited, with only preliminary investigations on one-dimensional gradient structures via the so-called pass-band splitting effects [58–60]. While these studies indicate that both structural asymmetry and bandgaps are essential for triggering asymmetric dynamic responses [58–60], the underlying mechanisms remain elusive. Furthermore, existing techniques face critical challenges in practical applications, such as complex fabrication of gradient structures, narrow operational bandwidths, and low transmission efficiency. Consequently, developing new theoretical frameworks and design strategies is imperative for creating broadband, efficient, and readily manufacturable unidirectional wave devices.

Motivated by this, a generalized finite mass-spring chain model is introduced to investigate the asymmetric response, characterized by unidirectional vibration transmissibility (UVT) under bidirectional excitation. The novelty of this work does not lie in the model itself, but in the novel physical insights and the general design principle derived from it. Section 2 elucidates the underlying mechanisms, establishing an explicit correlation between the transmissibility extrema and the eigenfrequencies of adjoint subsystems. Section 3 applies and validates the identified mechanisms through the design of a periodic beam featuring asymmetrical thickness profiles and wide bandgaps to achieve broadband and efficient UVT. Subsequently, Section 4 presents experimental results that corroborate both the observed UVT phenomena and corresponding theoretical predictions. Finally, conclusions are drawn synthesizing the key findings. This study provides a new and systematic framework for the design of broadband unidirectional elastic wave functional devices.

2. Universal spring-mass model for unidirectional vibration transmissibility

This section investigates a generalized spring-mass model to analyze UVT in both general and periodic chain systems. The objectives are to explore the underlying mechanisms of UVT and establish an explicit correlation between the transmissibility extrema and the eigenfrequencies of adjoint subsystems. The effect of structural asymmetry, boundary conditions, bandgaps, and structural unit-cell number on UVT is addressed through eigen analysis and transmissibility inspection.

2.1. UVT in a generalized n-dimensional spring-mass chain system

Consider a general n-dimensional spring-mass chain composed of n masses and n+1 springs, as illustrated in Fig. 1(a). The masses and the

springs can be adjusted to tailor the symmetry of the system, allowing for the investigation of UVT in this representative and general asymmetrical system. By fixing m_i , the (i-1)-dimensional subsystem is defined as the left-side system consisting of masses m_j with j smaller than i, while the (n-i)-dimensional complementary subsystem is the right-side system consisting of masses m_j with j larger than i. Specifically, the (n-1)-dimensional subsystem is defined as the system by fixing mass m_n , while the (n-1)-dimensional complementary subsystem corresponds to the system with fixed mass m_1 . Particularly, the n-dimensional subsystem or the complementary subsystem is the n-dimensional system itself. When subjected to an excitation force \mathbf{F} , the governing vibration equation of the n-dimensional system can be expressed as

$$\mathbf{M}\ddot{\mathbf{x}} + \mathbf{K}\mathbf{x} = \mathbf{F},\tag{1}$$

where $\mathbf{M} \equiv \mathrm{diag}[m_i], \mathbf{K} \equiv \mathrm{tridiag}[k_{ii}, k_{i,i+1}, k_{i+1,i}]$ with $k_{ii} = k_{i-1} + k_i$, $k_{i,i+1} = k_{i+1,i} = -k_i$. Considering a general case with the excitation applied at an arbitrary mass m_i , namely $\mathbf{F} = [0...0F_i0...0]$ sinot, and substituting the harmonic response $\mathbf{x} = \mathbf{X}$ sinotinto Eq. (1), one can get

$$\left[\mathbf{K} - \omega^2 \mathbf{M}\right] \mathbf{X} = \mathbf{F}.\tag{2}$$

Then, the displacement response **X** can be obtained by $\mathbf{X} = \mathbf{D}^{-1}\mathbf{F}$, where **D** is the eigenmatrix of the system, expressed as $\mathbf{D} \equiv \mathbf{K} - \omega^2 \mathbf{M} \equiv \text{tridiag} \left[D_{ii}, D_{i,i+1}, D_{i+1,i} \right] \text{ with } D_{ii} = k_{i-1} + k_i - m_i \omega^2, \ D_{i,i+1,} = D_{i+1,i} = -k_i.$ Specifically, the response of m_i, m_1 and m_n can be expressed as [61]

$$X_{ii} = F_i \Delta_{i-1} \delta_{n-i} / \Delta_n, \tag{3}$$

$$X_{1i} = F_i k_1 k_2 ... k_{i-1} \delta_{n-i} / \Delta_n, \tag{4}$$

$$X_{ni} = F_i k_i k_{i+1} ... k_{n-1} \Delta_{i-1} / \Delta_n, \tag{5}$$

where X_{ij} denotes the displacement amplitude of the mass m_i with the force applied on the mass m_i ; Δ_i or δ_i the characteristic determinant of the i-dimensional subsystem or complementary subsystem. $\Delta_n(\omega)=0$ corresponds to the eigenfrequencies of the n-dimensional system, at which all the displacement response approach infinity as deduced from Eqs. (3) to (5). Moreover, the displacement response X_{ii} vanishes at the eigenfrequencies of the (i-1)-dimensional subsystem or the (n-i)-dimensional complementary subsystem, i.e. $\Delta_{i-1}(\omega)=0$ or $\delta_{n-i}(\omega)=0$, as shown in Eq. (3). In another word, the anti-resonance frequencies with vanishing response at excitation point are equal to the eigenfrequencies of either the left-side (i-1)-dimensional subsystem or the right-side (n-i)-dimensional complementary subsystem with the mass at the excitation point being fixed.

The left and right vibration transmissibility from the excitation point

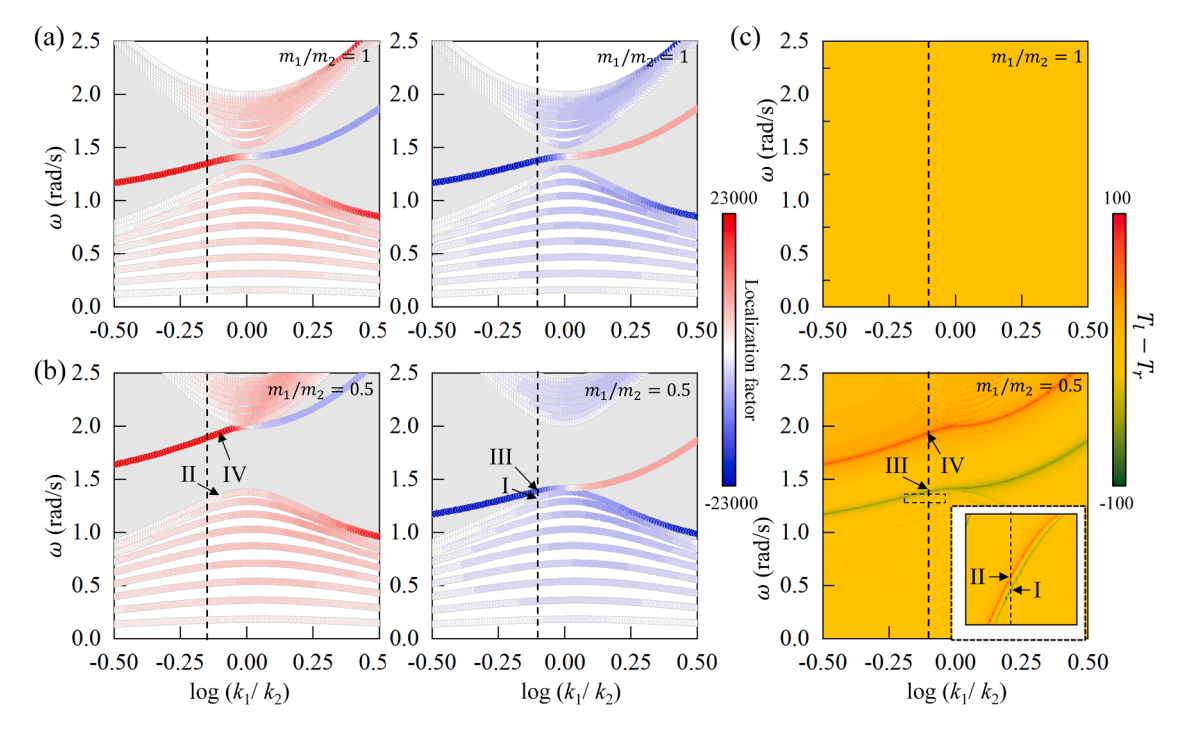


Fig. 2. (a) Symmetrical $(m_1/m_2 = 1)$ and (b) asymmetrical $(m_1/m_2 = 0.5)$ structure, eigenfrequencies of the subsystem (right panels) and the complementary subsystem (left panels), along with (c) the corresponding bilateral transmissibility differences, for varying spring stiffness ratios. The light grey areas correspond to the frequency range within bandgaps obtained in the infinite structures. The region with smaller dashed rectangular is enlarged as shown in the adjacent bigger dashed box.

can be respectively obtained through Eqs. (3) to (5) by

$$T_l = 20\log \frac{X_{ni}}{X_{ii}} = 20\log \frac{k_i k_{i+1} ... k_{n-1}}{\delta_{n-i}},$$
 (6)

$$T_r = 20\log \frac{X_{1i}}{X_{ii}} = 20\log \frac{k_1 k_2 ... k_{i-1}}{\Delta_{i-1}}.$$
 (7)

Apparently, the eigenfrequencies of the (n-i)-dimensional complementary subsystem with $\delta_{n-i}(\omega)=0$ correspond to the poles of the transmissibility function of the left-side excitation T_b while the eigenfrequencies of the (i-1)-dimensional subsystem with $\Delta_{i-1}(\omega)=0$ correspond to the poles of the transmissibility function of the right-side excitation T_r . In more detail, as can be seen from Eqs. (3) to (7), when the right-side (n-i)-dimensional complementary subsystem resonates $(\delta_{n-i}(\omega)=0)$, the displacement of both masses m_1 and m_i vanishes $(X_{1i}=X_{ii}=0)$, allowing vibration response exclusively from the excitation point to the right side with extremum value of T_l . Conversely, vibration is only observed on the left side to the excitation point when the left-side (i-1)-dimensional subsystem resonates $(\Delta_{i-1}(\omega)=0)$. This implies that tailoring the structural symmetry with different eigenfrequencies of the bilateral subsystems can achieve UVT.

To quantify the UVT efficiency, the difference between the left and right vibration transmissibilities is obtained by

$$T_l - T_r = 20\log \frac{X_{ni}}{X_{1i}} = 20\log \frac{k_i k_{i+1} \dots k_{n-1} \Delta_{i-1}}{k_1 k_2 \dots k_{i-1} \delta_{n-i}}.$$
 (8)

It can be observed that the bilateral transmissibility difference is intrinsically linked to the left and right springs separated by the excitation point, as well as the properties of the (i-1)-dimensional subsystem and the (n-i)-dimensional complementary subsystem. As such, any structural asymmetries in either mass distribution, stiffness configuration, or boundary conditions would result in the bilateral transmissibility difference and lead to UVT. Notably, as can be seen from Eqs. (8), the extremum values of the transmissibility difference coincide with the zeros of $\delta_{n-i}(\omega)$ or $\Delta_{i-1}(\omega)$, i.e. the eigenfrequencies of either the complementary subsystem or the subsystem. This correlation, which is

referred to as eigenfrequency-transmissibility correlation, facilitates the investigation of the vibration response under a specific excitation through eigenfrequency and eigenvector analyses of the corresponding subsystem and complementary subsystem.

Consider the special case, i.e. excitation and response are respectively applied and retrieved at the two ends of the spring-mass chain, the bilateral transmissibility difference writes

$$T_l - T_r = 20\log\frac{\Delta_{n-1}}{\delta_{n-1}}. (9)$$

Detailed derivation procedure can be referred to Appendix A. Similarly, the poles of the transmissibility difference equate to the eigenfrequencies of either the (n-1)-dimensional subsystem or complementary subsystem. The stronger the asymmetry between the subsystem and complementary subsystem is, the greater the transmissibility difference is.

2.2. UVT in a periodic spring-mass system

To further investigate the UVT of periodic asymmetrical structures and figure out how bandgap affects UVT, a periodic spring-mass system is analyzed. As shown in Fig. 1(b), masses m_1 and m_2 are periodically arranged by interconnecting springs k_1 and k_2 . The boundaries are modulated via the left and right springs k_L and k_R . Section 2.1 shows that the system's UVT behavior is intrinsically tied with the structural asymmetry of the subsystem and the complementary subsystems derived from fixing the excitation point. For subsequent analysis, the periodic unit count is set as N=10, with baseline parameters $m_2=1$ kg, $k_2=1$ N/m, and $k_R=1$ N/m. By modulating the mass ratios m_1/m_2 , and the spring stiffness ratios k_1/k_2 and k_L/k_R , the periodicity and the asymmetry of the system can by systematically control.

The eigenfrequencies and the corresponding eigenvectors of the subsystems can fully reflect the dynamic responses at the poles of displacement transmissibility, as demonstrated in Section 2.1. As such, the eigenfrequencies of the subsystem under right-side excitation and

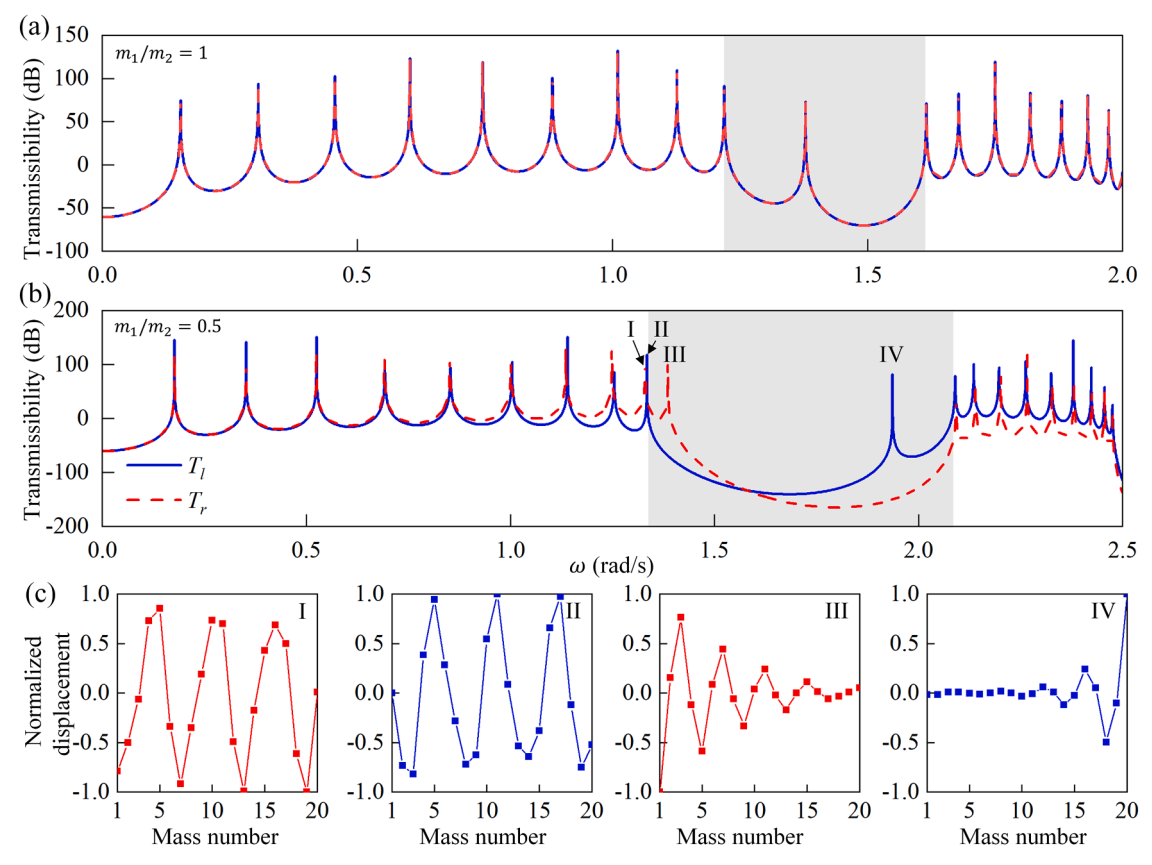


Fig. 3. Vibration transmissibility comparisons of (a) symmetrical $(m_1/m_2 = 1)$ and (b) asymmetrical $(m_1/m_2 = 0.5)$ structure at the condition of $k_1/k_2 = 10^{-0.1}$. (c) Normalized displacement at picked frequencies I-IV in Fig. 3(b).

the complementary subsystem under left-side excitation are employed to investigate the effects of the mass and stiffness ratios on the left and right vibration transmissibilities of the whole system, respectively, as shown in Fig. 3. The eigenfrequencies are color coded according to a localization factor P, which is defined as

$$P = \sum_{i=1}^{2N} L(i)Y_i, \tag{10}$$

with

$$L(i) = \begin{cases} -e^{N+1-i}, & i \le N \\ e^{i-N}, & i > N \end{cases} \in [1, 2N], \tag{11}$$

with Y_i being the i th element of the 2N*1 eigenvector. L(x) is a weight function. The value of P indicates the amplitude and direction of the mode localization, i.e., a larger P signifies the stronger rightward mode localization while a lower P signifies leftward localization. The bandgap ranges of the infinite system are shaded in light gray for reference.

When $m_1/m_2=1$, the systems remain mirror symmetric regardless of k_1/k_2 . The subsystem and its complementary subsystem are strictly equivalent, thus resulting in the same eigenfrequencies, as shown in the left and right panels of Fig. 2(a). According to the above-deduced eigenfrequency-transmissibility correlation, there will be no poles or zeros for the bilateral transmissibility difference as a result of the coinciding anti-resonances of Δ_{n-1} and δ_{n-1} in Eq. (9). This is further confirmed by the vanishing transmissibility differences calculated from Eqs. (A.6) and (A.11), as shown in the upper panel of Fig. 2(c).

However, for the asymmetric configuration $(m_1/m_2=0.5, {\rm Fig.~2(b)})$, the two eigenfrequencies diverge (Fig. 2(b)) and transmissibility difference appears (lower panel of Fig. 2(c)). Eq. (9) indicates that the eigenfrequency of the complementary subsystem coincides exactly with the maximum value of transmissibility difference, and the

eigenfrequency of the subsystem coincides with the minimum value, confirmed again by comparing Fig. 2(b) and the lower panel of Fig. 2(c).

Bragg scattering effects intensify with the increasing ratios of spring stiffness k_1/k_2 , broadening the bandgap width. The sign of localization factor changes around $k_1/k_2=1$, suggesting a shift of the localization position within bandgaps. Crucially, the localization intensity of the eigenvectors within the bandgaps of the (complementary) subsystem appears apparently higher than those within the bands as shown in Fig. 2 (a) and (b). The bandgaps act as a barrier to spatially cut off the vibrations between the two ends of the system and lead to such single-side localization. This also indicates the significance of wide bandgaps for the UVT with high localization.

A fixed spring stiffness ratio, $k_1/k_2 = 10^{-0.1}$ (marked by dashed line in Fig. 2) is selected to further show the corresponding transmissibility spectrum and displacement fields in Fig. 3. For the periodic symmetrical structure (Fig. 3(a)), the left and right transmissibility curves are identical. While for the periodic asymmetrical structure (Fig. 3(b)), UVT appears as the extrema of the transmissibility at peaks within both passband and bandgap. Within the passband, although the selected two peaks (peaks I and II) manifest the UVTs for the left-side and right-side excitation, respectively, the displacement fields tend to be uniform throughout the whole chain (left two panels of Fig. 3(c)), as a result of their strong couplings with the nearby vibrational modes of the chain. Such couplings are largely cut off when the modes are spectrally isolated by bandgaps. This leads to the high-localized displacement fields of peaks within bandgaps such as peaks III and IV as shown in the two right panels of Fig. 3(c). It again underscores the critical role of bandgaps in achieving high-performance asymmetric wave control.

Apart from the asymmetry that comes from every single unit cell, the asymmetry from the boundary conditions significantly alters the behavior of UVT as well. Compared with the case of symmetrical boundary condition ($k_{\rm L}=k_{\rm R}=1{\rm N/m}$ shown in the left panel of Fig. 4

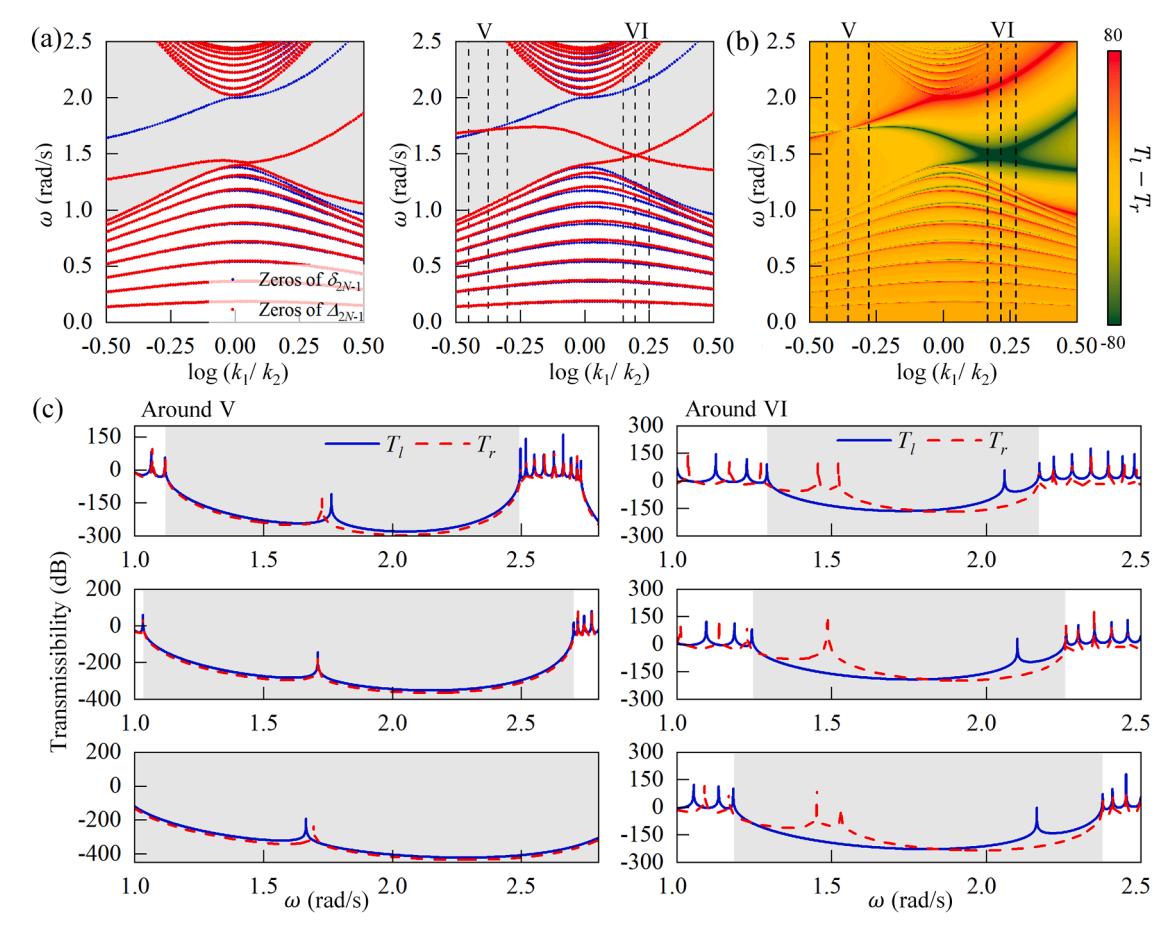


Fig. 4. Effect of asymmetry from the boundary conditions. When $m_1/m_2 = 0.5$ and $k_R = 1$ N/m, (a) the eigenfrequencies of the subsystem (red dash lines) and the complementary subsystem (blue dash lines) for symmetrical (left panel) and asymmetrical (right panel) boundary conditions with their k_L being 1 N/m and $10^{0.4}$ N/m, respectively. (b) The spectrum of the bilateral transmissibility differences as $\log(k_1/k_2)$ ranging from -0.5 to 0.5. The color denotes magnitude of the difference. (c) The selected spectrum of vibration transmissibility around point V with $\log(k_1/k_2)$ being -0.375 (middle), -0.45 (bottom), as well as point VI with $\log(k_1/k_2)$ being 0.15 (top), 0.196(middle), 0.25(bottom), which correspond to the dashed lines in (a) and (b).

(a)), the asymmetrical case ($k_{\rm L} = 10^{0.4}$, $k_{\rm R} = 1$ N/m shown in the right panel of Fig. 4(a)) yields intriguing phenomenon such as the vanishment and the merging of UVT. On one hand, the effect induced by boundary asymmetry can be neutralized by structural asymmetry; this would lead to the equal value of eigenfrequencies of the subsystem and complementary subsystem (e.g., point V marked in the right panel of Fig. 4(a)) and result in the vanishment of UVT (Fig. 4(b)). The left panel of Fig. 4 (c) further showcase how vibration transmissibility evolves at specific spring stiffness ratios around point V (marked with dashed line in Figs. 4 (a) and (b)). At point V, left and right transmissibility peaks coincide, and their difference no longer attains local extrema within the bandgap range. On the other hand, UVT can also be reinforced at specific spring stiffness ratios (e.g., point VI). The multiple subsystem eigenfrequencies can merge to broaden the operational bandwidth of the unidirectional wave control, as demonstrated in Fig. 4(b) and the right panel of Fig. 4 (c).

The strong dependence of the transmissibility magnitude (i.e., UVT efficiency) on structural unit-cell number should be particularly emphasized, as demonstrated in Fig. 5. With the number of unit cells increasing, as shown in Figs. 5(a) to 5(c), eigenfrequencies of the subsystems remain different from those of the complementary subsystems, indicating the persistence of UVT regardless of unit-cell number. Notably, the eigenfrequencies within bandgaps remain invariant, which is attributed to the high-localized displacement fields insensitive to the unit-cell number, and further confirmed by the invariant peak frequencies of bilateral transmissibility within bandgaps shown in Fig. 5 (d). However, both the left and right transmissibility magnitudes within

the bandgaps reduce due to the bandgap-induced vibration attenuation. Excessive number of unit cells (egs. N=10 and N=20) would significantly reduce the UVT efficiency that challenges practical engineering applications. Consequently, except for the periodic asymmetrical structural unit itself, the number of unit cell should also be meticulously designed to achieve highly efficient UVT.

3. Application and validation in continuous systems

In Section 2, discrete spring-mass systems are examined to demonstrate that UVT intrinsically originates from the structural symmetry and is governed by an eigenfrequency-transmissibility correlation. This section extends this theoretical framework to continuous structures by designing and analyzing a periodic beam with intentional asymmetry. The primary objective is to examine whether the established eigenfrequency-transmissibility correlation persists in continuous systems and to explore how this correlation contributes to efficient UVTs.

To determine whether this correlation persists in continuous systems, a periodic beam is designed to incorporate two critical parameters identified in Section 2: strong structural asymmetry and broad bandgaps. This beam serves as a continuous realization of the discrete model studied previously, wherein the spatial variation in thickness corresponds to the intentional non-uniformity of masse and spring elements in the spring-mass chain model. Specifically, the local mass per unit length is proportional to the cross-sectional area, which depends on the local thickness, while the local bending stiffness analogous to the spring stiffness with the scale proportional to the cube of the thickness,

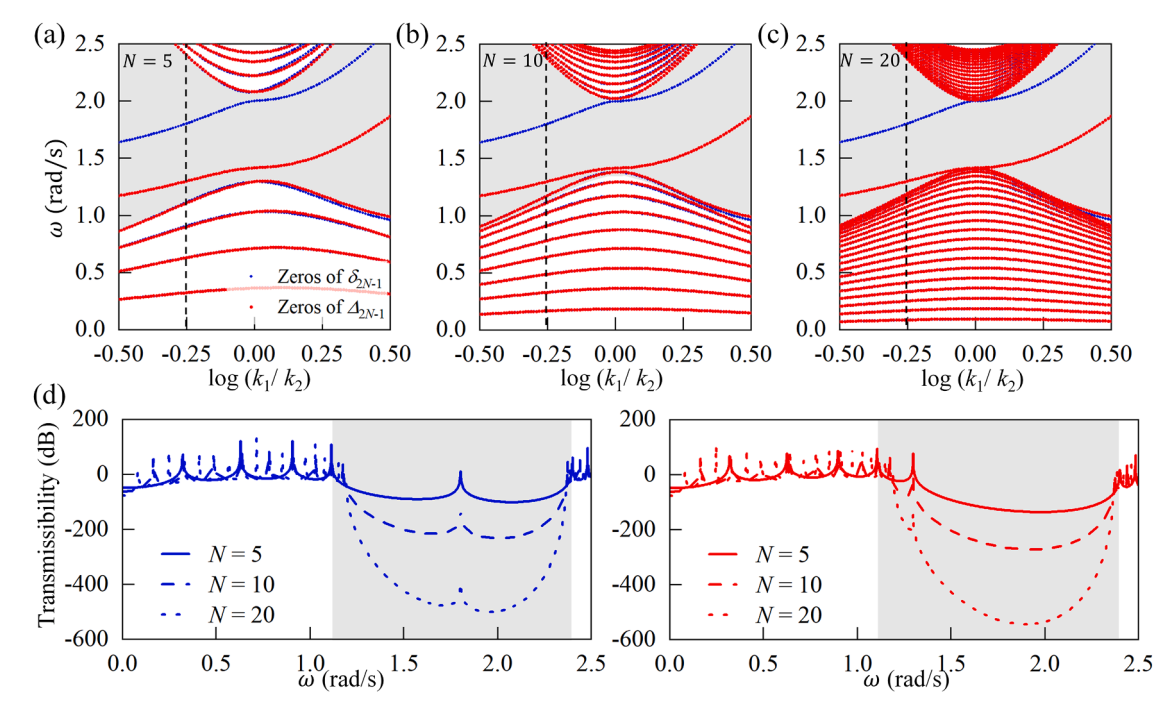


Fig. 5. Effect of structural unit-cell number. When $m_1/m_2 = 0.5$ and $k_L = k_R = 1$ N/m, the eigenfrequencies of the subsystem (red dash lines) and the complementary subsystem (blue dash lines) for different unit cells with (a) N = 5, (b) N = 10, and N = 20, respectively. (d) Left (left panel) and right (right panel) transmissibility comparison for different unit cells at the condition of $k_1/k_2 = 10^{-0.25}$.

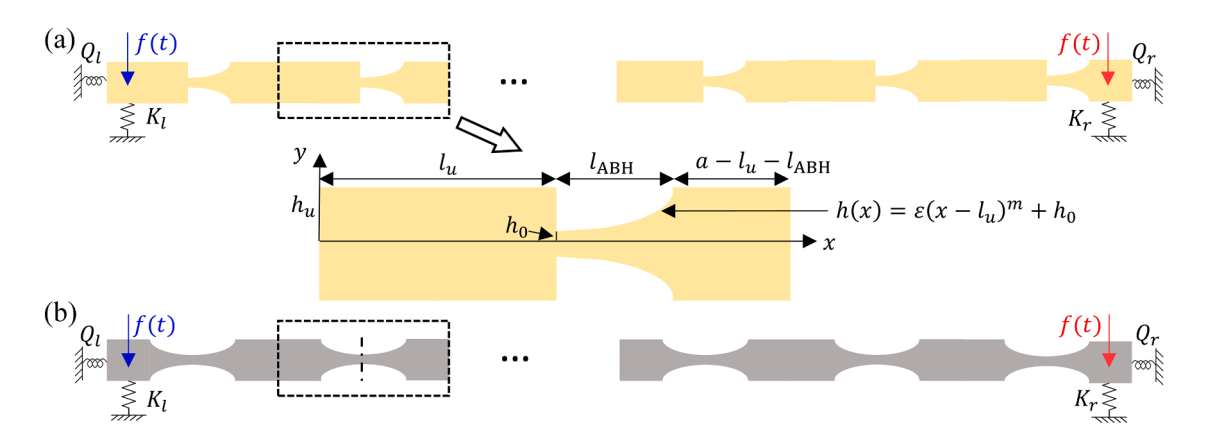


Fig. 6. Sketch of periodic beams with (a) asymmetrical single ABH indentation and (b) two symmetrical ABH indentations: two ends of beams are supported by translational and rotational springs to mimic various boundary conditions.

according to Euler-Bernoulli beam theory. Consequently, a beam with spatially varying thickness effectively introduces continuous distributions of mass and stiffness, thus mirroring the deliberate variation of masses and springs in the discrete model. This continuous-discrete analogy helps intuitively understand the origin of UVT in continuous structures so that the same design framework can be applied to achieve enhanced UVT.

As depicted in Fig. 6(a), the unit cell (length a) features a uniform left segment (thickness $2h_{\rm u}$, length $l_{\rm u}$), a thickness-varying middle segment (length $l_{\rm ABH}$), and a uniform right segment (length a- $l_{\rm u}$ - $l_{\rm ABH}$). The middle segment follows a power-law thickness profile $h(x) = \varepsilon (x-l_{\rm u})^m + h_0$, which is a highly asymmetrical configuration, characteristic of the so-called Acoustic Black Hole (ABH) structures [62–68]. This design enables precise tuning of left-right asymmetry by adjusting segment lengths. Critically, periodic beam [69–77] or plate [78–83] structures with ABH elements have been shown to entail broadband bandgaps through combined local resonances and Bragg scattering mechanisms.

For reference, Fig. 6(b) shows a symmetrical counterpart with paired ABH profiles.

Consider a free finite beam comprising three unit cells under left-side or right-side excitation, respectively. Our previously developed wavelet-decomposed and energy-based model [68,69] is applied to calculate the vibration transmissibility of a finite structure and the band structures of an infinite system. The modeling principle is briefly recalled in Appendix B for the benefit of readers. The thickness of the uniform beam portion $2h_u$ and the length a of the unit cell are set to be 0.32 cm and 8 cm, respectively. The ABH profile features length $l_{abh}=2$ cm, truncation thickness $h_0=0.02$ cm and m=2. The length $l_{\rm u}$ of the asymmetrical beam is zero. The material is steel with a mass density of 7800 kg/m³, Young's modulus of 210 GPa, and damping loss factor of 0.001.

Analogous to discrete systems, the subsystem and complementary subsystem of the continuous systems are respectively defined when its left-side and right-side ends are pinned. Fig. 7(a) presents the eigenfrequencies of these subsystems and complementary subsystems for

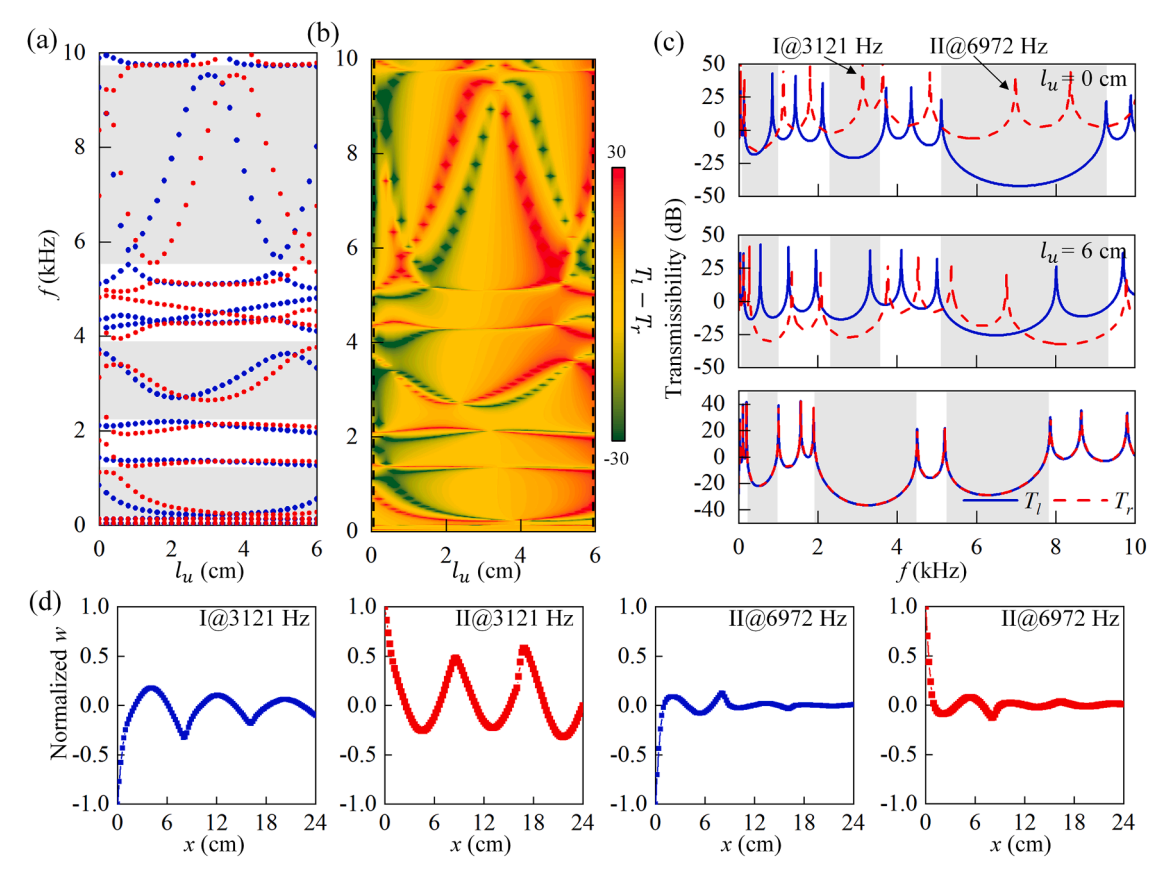


Fig. 7. (a) Eigenfrequencies of the subsystem (right-side excitation, red dots) and the complementary subsystem (left-side excitation, blue dots) for varying l_u . (b) The corresponding bilateral transmissibility differences and (c) transmissibility comparisons at the condition of $l_u = 0$ cm (top), $l_u = 6$ cm (middle), and the referenced symmetrical beam (bottom). (d) Normalized displacement responses at two resonant frequencies I@3121 Hz and II@6972 Hz as marked in (c).

periodic asymmetrical ABH structures with varying asymmetry levels (controlled by l_u). A comparison with bilateral transmissibility differences in Fig. 7(b) shows that the maxima of these differences align well with the complementary subsystem eigenfrequencies and the minima with the subsystem eigenfrequencies. This confirms that the

eigenfrequency-transmissibility correlation established for discrete systems can be well extended to continuous systems.

The discrepancy between the eigenfrequencies of subsystems and their complementary counterparts would lead to UVT. Such discrepancy generally originates from the asymmetry from structure itself or

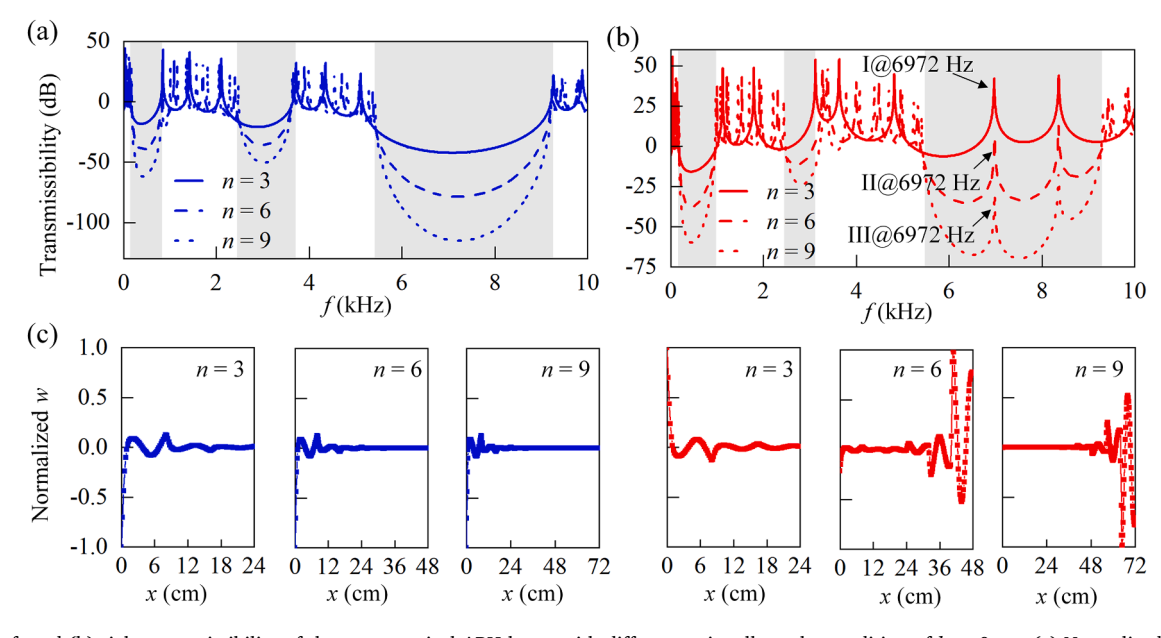


Fig. 8. (a) Left and (b) right transmissibility of the asymmetrical ABH beam with different unit cells at the condition of $l_u = 0$ cm. (c) Normalized displacement responses at picked frequencies for the beam with different cells, respectively.

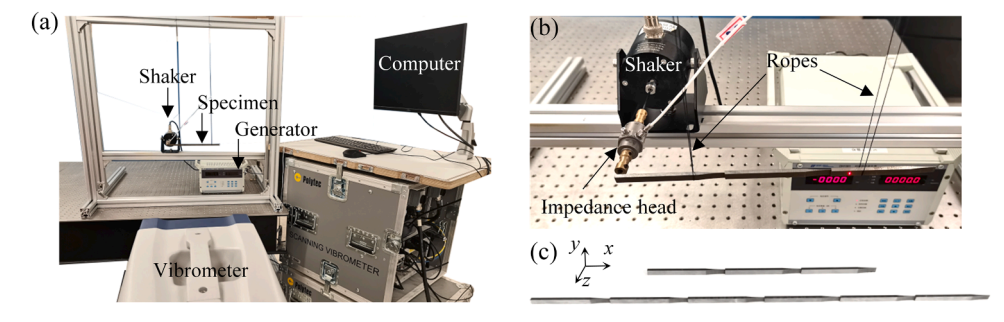


Fig. 9. Experimental setup: (a) overall diagram; (b) partial detail; (c) specimens with three- and six-unit cells respectively.

boundary condition. In Fig. 7(a), as l_u increases from 0 to 6 cm, the bandgap range of the infinite structure remains invariant, whereas the asymmetry difference decreases and then increases. The stronger asymmetry (e.g., $l_u=0$ cm or 6 cm) generates more pronounced broadband asymmetric transmission. Moreover, consistent with discrete systems, transmissibility differences within bandgaps exhibit significantly greater magnitude, thus conducive to more efficient UVT, as shown in Fig. 7(c). It is noteworthy that asymmetrical ABH beams with varying asymmetry levels can exhibit identical bandgaps despite their markedly different UVT behaviors in finite configurations, which necessitates the proposed eigenfrequency-transmissibility correlation specially for the dynamics of the finite asymmetric systems.

Moreover, as suggested by Eq. (8) and the analysis of the boundary condition effects on UVTs in the discrete system (Fig. 4), even under

symmetric boundary conditions, the structural asymmetry introduced by the ABH design suffices to achieve significant UVT. This flexibility allows for maintaining the UVT functionality with different boundary constraints. Therefore, by tuning internal geometric parameters such as $l_{\rm u}$, the UVT behavior can be optimized irrespective of external boundary conditions, enhancing its applicability in various real-life engineering contexts.

Fig. 7(c) further presents the transmissibility spectra for different l_{u} . For asymmetrical beams, left-side excitation transmissibility (T_l) exhibits fundamentally distinct behavior from right-side excitation (T_r), a hallmark of UVT, contrasting sharply with the identical responses in the symmetrical case. Specifically, varying the asymmetry parameter (l_u) between 0 cm and 6 cm permits the tuning of both effective UVT frequencies and transmission efficiency, the latter being significantly

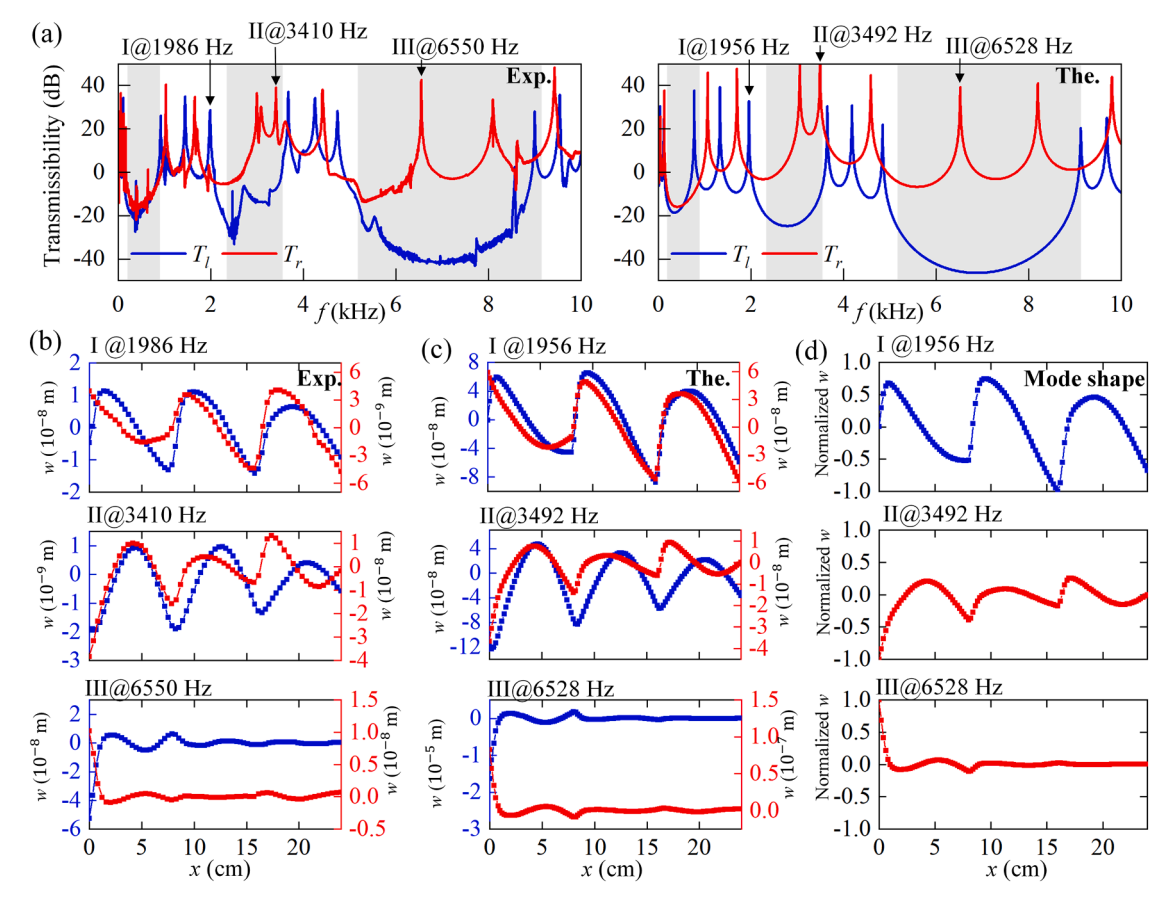


Fig. 10. (a) Experimental (left) and theoretical (right) transmissibility of the beam with three asymmetrical ABH cells under left-side and right-side excitations, respectively; (b) experimental and (c) theoretical displacement responses at selected frequencies I (top), II (middle), III (bottom) marked in (a); (d) corresponding theoretical mode shape of the subsystem (right-side excitation, red dots) and the complementary subsystem (left-side excitation, blue dots).

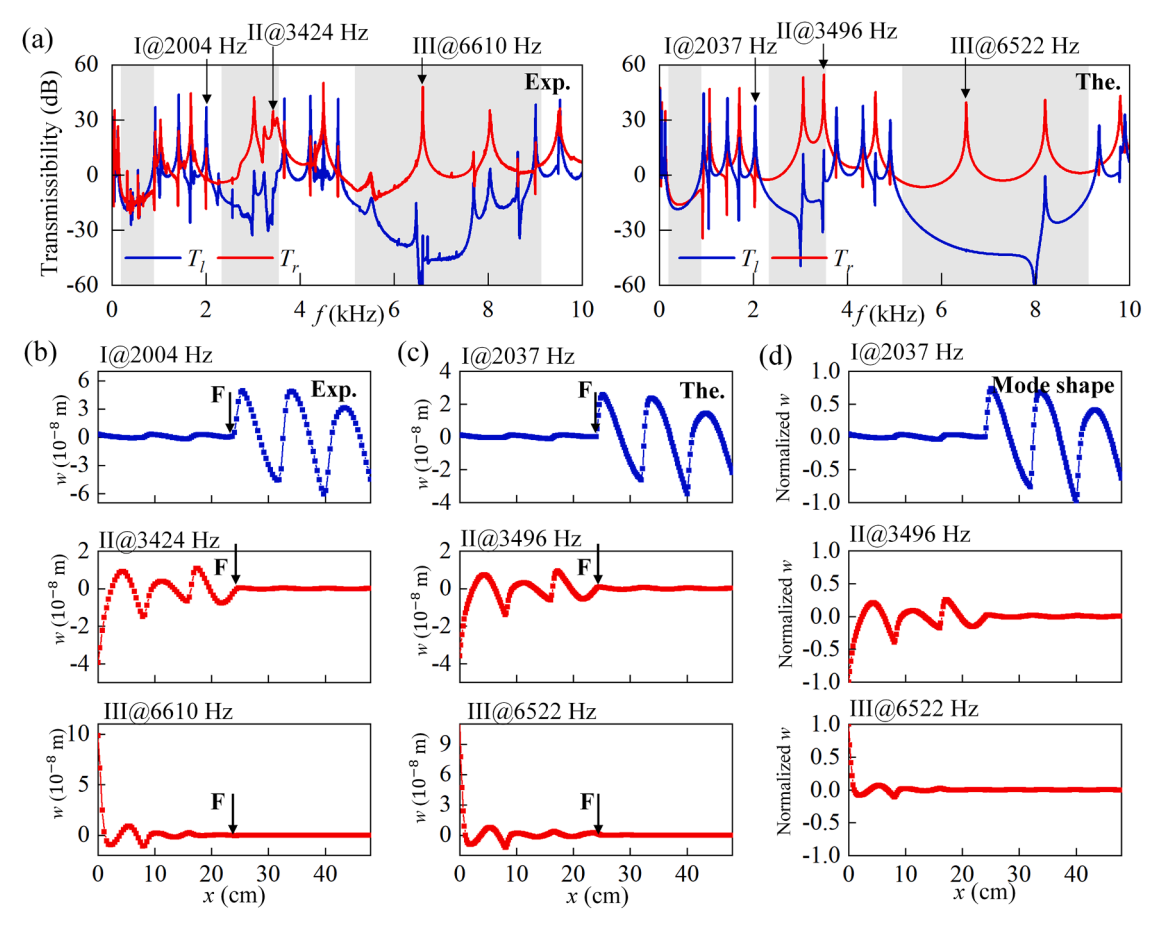


Fig. 11. (a) Experimental (left) and theoretical (right) transmissibility of the beam with six cells under middle point excitation; (b) experimental and (c) theoretical displacement responses at selected frequencies I (top), II (middle), III(bottom) in (a); (d) corresponding theoretical mode shape of the subsystem and complementary subsystem.

enhanced within bandgaps. When $l_u=0$, within the second and third broadband bandgap ranges (2544~3613 Hz and 5467~9240 Hz), T_l remains below -20 dB, demonstrating significant vibration attenuation, while T_r predominantly exceeds 0 dB and even manifests multiple resonance peaks, indicative of vibration amplification instead of attenuation. Normalized displacement responses at two resonant frequencies (shown in Fig. 7(d)) confirm this directional asymmetry that vibrations attenuate rapidly under left-side excitation but amplify substantially under right-side excitation. Remarkably, this asymmetrical periodic ABH beam achieves over 20 dB directional transmissibility differences across a broad frequency range up to 4500 Hz.

The dependence of the transmissibility magnitude on structural unit-cell number is also revisited in the continuous system scenario, as demonstrated in Fig. 8. Consistent with discrete systems, UVT functionality persists with increasing unit cells, yet bandgap-induced attenuation markedly reduces the bilateral transmissibility magnitudes within bandgap regions. Notably, although the peak frequencies of the right transmissibility remain invariant (see representative points II and III), the magnitude evolves from vibration amplification (n=3) to strong attenuation (n=9), indicating severe UVT efficiency degradation. This efficiency reduction is corroborated by normalized displacement responses for different unit cells, as shown in Fig. 8(c). The invariant peak frequencies stem from the localized displacement field's insensitivity to unit-cell quantity.

4. Experimental validation

This section describes experiments designed to validate the aforementioned UVT and examine the proposed correlation between the measured transmissibility spectra and the calculated eigenfrequencies of subsystems/complementary subsystems. Tests are performed on two steel beams with three and six asymmetric ABH unit cells under free boundary conditions. Using swept-sine excitation and laser vibrometer measurement, bilateral vibration transmissibility and displacement fields are measured.

As shown in Fig. 9(c), two tested beams are processed by wire cutting with steel material, with a mass density of 7657 kg/m³, Young's modulus of 200 GPa, and damping loss factor of 0.001. Their geometrical parameters are: $h_u = 0.16$ cm, a = 8 cm, $l_{abh} = 2$ cm, $h_0 = 0.019$ cm, m = 2.15, $l_u = 0$. The tested beam is suspended by two thin strings to mimic free boundaries. An electromagnetic shaker (East China Testing DH40020) is used to excite the beam at either end depending on the test requirement. The shaker is driven by a sinusoidal signal sweeping from 0 to 10 kHz generated by a signal generator (East China Testing DH1301). A Polytec scanning laser vibrometer (PSV-500 HR) is used to scan the whole beam for response measurement. The force is measured through an impedance head (Kistler 8770A5) with the measured signal fed back to the laser vibrometer as reference.

Fig. 10 presents a comparison of the vibration transmissibility of the

three-unit asymmetrical ABH beam under left-side and right-side excitations. Distinct differences in bilateral vibration transmissibility are observed across a broad frequency range, particularly within the bandgap ranges of 2330~3564 Hz and 5152~9133 Hz. Notably, the transmissibility under the right-side excitation exceeds 0 dB and surpasses left-side excitation transmissibility by over 20 dB, demonstrating an efficient broadband UVT of the tested asymmetrical ABH. Moreover, in terms of the measured displacement field at peaks, those peaks isolated within bandgaps (such as peak III) show largely localized feature than those peaks close to the band (peak I and II), as compared in Fig. 10 (b), consistent with the spring-mass model developed in Section 2 as well. Those experimental results exhibit good agreement with the theoretical calculations, both in terms of transmissibility (right panel of Fig. 10(a)) and displacement field (Fig. 10(c)), thus validating the theoretical framework proposed in Section 2. To further validate the derived eigenfrequency-transmissibility correlation, the eigenfrequencies and modal shapes of the subsystem and the complementary subsystem of the beam are calculated and shown in Fig. 10(d). The eigenfrequencies agree well with the corresponding peak frequencies, while the mode shapes are also aligned with the displacement field, providing the direct supporting evidence. Note minor discrepancies between the measured and calculated results are observed which can be primarily attributed to three factors. First, machining error occurs when achieving the ultrathin ABH thickness profile. Second, the inevitable deviation of the excited force from the central axis would cause torsional effect, which is neglected in the theoretical model. Finally, challenges arise in accurately measuring the subtle vibration within the bandgap range during experiments.

Experiments also show that the above UVT phenomena appear more intuitive when the number of unit cell is double with excitation applied at the central point of ABH beam. In this case, the UVT is directly reflected through one single excitation by investigating the contrast vibration transmissibility (Fig. 11(a)) and displacement fields (Fig. 11(b)) of the left and right parts of the six-unit asymmetric ABH. More specifically, Fig. 11(b) shows that, at peak I, the displacement field within the right part is significantly larger than that within the left part, while at peaks II and III, the situation reverses. Once again, the experimental results are consistent with the theoretical calculations (right panel of Fig. 11(a) and Fig. 11(c)). Meanwhile, both the eigenfrequencies and mode shapes of the subsystem and the complementary subsystem comply to the eigenfrequency-transmissibility correlation.

5. Conclusions

In this study, a theoretical framework governing the occurrence of UVT in asymmetric finite structures is established. The core finding is the eigenfrequency-transmissibility correlation, a principle that is derived from a spring-mass chain model which, owing to its generality, is shown to pinpoint the intrinsic physical behavior of more general

continuous systems. This correlation demonstrates that the extrema of bilateral transmissibility occur at the anti-resonance frequencies with vanishing response at the excitation point, strictly corresponding to the eigenfrequencies of the adjoint subsystem or complementary subsystem with the excitation point fixed. It provides a universal explanation for UVT phenomena and shows that UVT arises from structural asymmetry (mass, stiffness or boundary conditions). Furthermore, the way in which UVT occurs in periodic systems and interacts with bandgaps is elucidated, demonstrating the crucial role that bandgaps play in modulating the bandwidth and efficiency of UVT.

Guided by this theoretical principle, a periodic continuous beam with ABH indentations is designed, fabricated and measured. Such structure inherently offer strong asymmetry and broadband bandgaps, which contribute to the experimentally measured over 20 dB bilateral transmission difference across a 4500 Hz bandwidth, in agreement with the theoretical prediction.

Although developed using a discrete model, the eigenfrequency-transmissibility correlation serves as a universal principle applicable to any linear asymmetric systems, continuous or discrete. This work addresses the challenge of designing finite structures for unidirectional transmission by providing a predictive theory and a general design framework. Future work will focus on extending this principle to more complex and practical structures, e.g., plates, trusses and exploring its applications for vibration control or energy harvesting in more practical engineering scenarios.

CRediT authorship contribution statement

Liling Tang: Writing – original draft, Methodology, Investigation, Funding acquisition, Formal analysis, Conceptualization. Shuowei An: Writing – review & editing, Visualization, Methodology, Investigation, Formal analysis, Conceptualization. Yuguang Chen: Validation, Investigation, Data curation. Debin Li: Validation, Data curation. Li Cheng: Writing – review & editing, Supervision, Methodology, Conceptualization.

Declaration of competing interest

The authors declare that they have no known competing financial interests or personal relationships that could have appeared to influence the work reported in this paper.

Acknowledgements

This work was supported by the Guangdong Basic and Applied Basic Research Foundation (No. 2024A1515011511), and the Opening Project from State Key Laboratory for Strength and Vibration of Mechanical Structures (No. SV2023-KF-16).

Appendix A Bilateral transmissibility for excitation and response at two ends of the spring-mass chain

With an excitation force applied at the left mass m_1 , namely $\mathbf{F} = [F_1 0...0]' \sin \omega t$, the response of m_1 and m_n , as well as the left vibration transmissibility can be respectively expressed as

$$X_{11} = F_1 \delta_{n-1} / \Delta_n, \tag{A.1}$$

$$X_{n1} = F_1 k_1 k_2 \dots k_{n-1} / \Delta_n, \tag{A.2}$$

$$T_{l} = 20\log \frac{X_{n1}}{X_{11}} = 20\log \frac{k_{1}k_{2}...k_{n-1}}{\delta_{n-1}}.$$
(A.3)

Eq. (A.1) shows that the anti-resonance frequencies of X_{11} equal to the eigenfrequencies of the (n-1)-dimensional complementary subsystem with $\delta_{n-1}(\omega)=0$. Moreover, they also correspond to the poles of transmissibility of the left-side excitation T_l .

Similarly, when a harmonic excitation is applied on the right mass m_n , namely $\mathbf{F} = [0...0F_n]'\sin\omega t$, the displacement response and the right vibration transmissibility write

L. Tang et al.

$$X_{1n} = F_n k_1 k_2 \dots k_{n-1} / \Delta_n,$$
 (A.4)

$$X_{nn} = F_n \Delta_{n-1} / \Delta_n, \tag{A.5}$$

$$T_r = 20\log\frac{X_{1n}}{X_{nn}} = 20\log\frac{k_1k_2...k_{n-1}}{\Delta_{n-1}}.$$
(A.6)

Analogously, the eigenfrequencies of the (n-1)-dimensional subsystem with $\Delta_{n-1}(\omega)=0$ are equivalent to the poles of transmissibility of the right-side excitation.

Appendix B Theoretical model for continuous beam systems

Based on the Euler-Bernoulli beam theory, the displacement field of the beam is expressed as $\{u,w\} = \left\{-z\frac{\partial w}{\partial x},w(x,t)\right\}$, with the flexural displacement w being expanded by Mexican Hat Wavelets (MHW) $\varphi_{i,s}(x)$ as

$$w(x,t) = \sum_{i=0}^{h} \sum_{s} a_{i,s}(t) \varphi_{i,s}(x),$$
(B.1)

where i and s being the scaling and translation parameter of the MHW.

The Lagrangian of the system writes

$$L = E_k - E_p + W, \tag{B.2}$$

where E_k denotes the kinetic energy of the system; E_p the potential energy and W the work done by excitation forces. They can be obtained, respectively, by

$$E_{k} = \frac{1}{2} \int^{\rho} \left(\frac{\partial w}{\partial t} \right)^{2} dV, \tag{B.3}$$

$$E_{p} = \frac{1}{2} \int^{E} I(x) \left(\frac{\partial^{2} w}{\partial x^{2}} \right)^{2} dx + \frac{1}{2} K_{l} w(x_{l}, t)^{2} + \frac{1}{2} Q_{l} \left(\frac{\partial w(x_{l}, t)}{\partial x} \right)^{2} + \frac{1}{2} K_{r} w(x_{r}, t)^{2} + \frac{1}{2} Q_{r} \left(\frac{\partial w(x_{r}, t)}{\partial x} \right)^{2},$$
(B.4)

$$W = f(t) \cdot w(x_f, t). \tag{B.5}$$

Applying the Lagrange's equations $\frac{d}{dt} \left(\frac{\partial L}{\partial \hat{q}_{l,s}(t)} \right) - \frac{\partial L}{\partial a_{l,s}(t)} = 0$ in the harmonic regime, one can get the vibration response of the structure by solving the following matrix equation

$$[\mathbf{K} - \omega^2 \mathbf{M}] \mathbf{A} = \mathbf{F},\tag{B.6}$$

with K and M being the stiffness and mass matrices, respectively; A and F being the vectors of the response and the excitation force, respectively. Setting the force vector in Eq. (B.6) to zero leads to the following eigenvalue equation

$$\mathbf{M}^{-1}\mathbf{K}\mathbf{A} = \omega^2 \mathbf{A},\tag{B.7}$$

which gives the eigenfrequencies and the corresponding mode shape functions.

For an infinite system, with consideration of periodic boundary conditions, i.e. $w_{n+1}(x+a) = e^{ika}w_n(x)$ and $w''_{n+1}(x+a) = e^{ika}w''_n(x)$, the Lagrangian of the whole system can be obtained by the sum of Lagrangians of every unit cell as

$$L = \sum_{n=-\infty}^{+\infty} L_n = L_n \sum_{n=-\infty}^{+\infty} e^{2qjka}. \tag{B.8}$$

Therefore, the Lagrange's equations of the entire infinite system can be expressed in terms of the Largrangians of one unit cell as

$$\frac{d}{dt}\left(\frac{\partial L_n}{\partial \dot{a}_{i,s}(t)}\right) - \frac{\partial L_n}{\partial a_{i,s}(t)} = 0. \tag{B.9}$$

Namely, the band structure of an infinite system can be obtained by solving the Lagranges's equations of one unit cell. Submitting the displacement expression with the periodic boundary conditions $w_n(a) = e^{jka}w_n(0)$ and $w'_n(a) = e^{jka}w_n(0)$ into Eq. (B.9), a matrix equation similar to Eq. (7) can be obtained. Sweeping the wave vector k along the irreducible Brillouin zone from $0 \cot a$, the corresponding eigenfrequencies and mode shape functions can be obtained. Details can be referred to Ref. [69].

Data availability

Data will be made available on request.

References

- [1] Nassar H, Yousefzadeh B, Fleury R, Ruzzene M, Alù A, Daraio C, Norris AN, Huang GL, Haberman MR. Noreciprocity in acoustic and elastic materials. Nat Rev 2020;5:667–85.
- [2] Liang B, Yuan B, Cheng JC. Acoustic diode: rectification of Acoustic energy flux in one-dimensional systems. Phys Rev Lett 2009;103(10):104301.
- [3] Liang B, Guo XS, Tu J, Zhang D, Cheng JC. An acoustic rectifier. Nat Mater 2010;9 (12):989–92.
- [4] Popa BI, Cummer SA. Non-reciprocal and highly nonlinear active acoustic metamaterials. Nat Commun 2014;5(1):3398.
- [5] Luo BB, Gao S, Liu JH, Mao YW, Li YF, Liu XZ. Non-reciprocal wave propagation in one-dimensional nonlinear periodic structures. AIP Adv 2018;8(1):015113.
- [6] Zhou W, Wang YZ. Metamaterial robot driven by nonlinear elastic waves with stop band and nonreciprocal crawling. Nonlinear Dyn 2024;112:5825–45.
- [7] He JS, Zhou JX, Wang K, Wang Q. Design of qusi-zero-stiffness elastic diodes for low-frequency nonreciprocity through machine learning. Acta Mech Sin 2024;40: 523461.
- [8] Wei LS, Wang YZ, Wang YS. Nonreciprocal transmission of nonlinear elastic wave metamaterials by incremental harmonic balance method. Int J Mech Sci 2020;173: 105433.
- [9] Wang R, Han L, Zhang MN, Wang LF, Huang QA. Perturbation-induced nonreciprocal transmission in nonlinear partity-time-symmetric silicon micromechanical resonators. Commun Phys 2025;8:21.
- [10] Luo HH, Bu XZ, Huang HB, Chen JJ. Tunable non-reciprocity of elastic waves in one-dimensional magnetoelastic phononic crystal plate with oblique incident angle. Phys Lett A 2024;499:129356.
- [11] Fleury R, Sounas DL, Sieck CF, Haberman MR, Alù A. Sound isolation and giant linear nonreciprocity in a compact acoustic circulator. Science 2014;343(6170): 516–9.
- [12] Zangeneh-Nejad F, Fleury R. Doppler-based acoustic gyrator. Appl Sci 2018;8(7): 1083.
- [13] Wiederhold CP, Sounas DL, Alù A. Nonreciprocal acoustic propagation and leakywave radiation in a waveguide with flow. J Acoust Soc Am 2019;146(1):802–9.
- [14] Shen C, Li J, Jia Z, Xie Y, Cummer SA. Nonreciprocal acoustic transmission in cascaded resonators via spatiotemporal modulation. Phys Rev B 2019;99(13): 134306.
- [15] Oudich M, Deng Y, Tao M, Jing Y. Space-time phononic crystals with anomalous topological edge states. Phys Rev Res 2019;1(3):033069.
- [16] Zhu XH, Li JF, Shen C, Peng XY, Song AL, Li LQ, Cummer SA. Non-reciprocal acoustic transmission via space-time modulated membranes. Appl Phys Lett 2020; 116(3):034101.
- [17] Attarzadeh MA, Al Ba'ba'a H, Nouh M. On the wave dispersion and non-reciprocal power flow in space-time traveling acoustic metamaterials. Appl Acoust 2018;133: 210.4
- [18] Trainiti G, Ruzzene M. Non-reciprocal elastic wave propagation in spatiotemporal periodic structures. New J Phys 2016;18(8):083047.
- [19] Khanikaev AB, Fleury R, Mousavi SH, Alù A. Topologically robust sound propagation in an angular-momentum-biased graphene-like resonator lattice. Nat Commun 2015;6(1):8260.
- [20] Yang ZJ, Gao F, Shi XH, Lin X, Gao Z, Chong YD, Zhang BL. Topological acoustics. Phys Rev Lett 2015;114(11):114301.
- [21] Lu ZX, Chen H, Yao LY. Investigation of unidirectional vibration isolation and nonreciprocal design of axial elastic waves based on topological pumping theory. Int J Solids Struct 2025;309:113192.
- [22] Gao YQ, Wang LF, Lu TJ. Coding non-Hermitian metamaterial beams based on nonlocal feedback control. Int J Mech Sci 2025;286:109904.
- [23] Banerjee A, Bera KK. Emergence of non-reciprocity in metabeam exploiting piezoelectric sensing and actuation. Int J Mech Sci 2025;286:109904.
- [24] Li RQ, Liang B, Li Y, Kan WW, Zou XY, Cheng JC. Broadband asymmetric acoustic transmission in a gradient-index structure. Appl Phys Lett 2012;101(26):263502.
- [25] Guan YJ, Sun HX, Xia JP, Yuan SQ. Broadband asymmetric acoustic transmission in a single medium by an array of heat sources. J Phys D: Appl Phys 2017;50(16): 165102.
- [26] Li Y, Liang B, Gu ZM, Zou XY, Cheng JC. Unidirectional acoustic transmission through a prism with near-zero refractive index. Appl Phys Lett 2013;103(5): 053505
- [27] Shen C, Xie YB, Li JF, Cummer SA, Jing Y. Asymmetric acoustic transmission through near-zero-index and gradient-index metasurfaces. Appl Phys Lett 2016; 108(22):223502.
- [28] Xu S, Qiu C, Liu Z. Acoustic transmission through asymmetric grating structures made of cylinders. J Appl Phys 2012;111(9):094505.
- [29] Li Y, Shen C, Xie YB, Li JF, Wang WQ, Cummer SA, Jing Y. Tunable asymmetric transmission via lossy acoustic metasurfaces. Phys Rev Lett 2017;119:035501.
- [30] Li B, Hu YB, Chen JL, Su GY, Liu YQ, Zhao MY, Li Z. Efficient asymmetric transmission of elastic waves in thin plates with lossless metasurfaces. Phys Rev Appl 2020;14:054029.
- [31] Hu YB, Zhang YH, Su GY, Zhao MY, Li B, Liu YQ, Li Z. Realization of ultrathin waveguides by elastic metagrating. Commun Phys 2022;5:62.

- [32] Chen L, Zhang CZ, Nie GH. One-way transmission of elastic waves in phononic beams. Int J Mech Sci 2025;297-298:110377.
- [33] Zhu XF, Zou XY, Liang B, Cheng JC. One-way mode transmission in onedimensional phononic crystal plates. J Appl Phys 2010;108(12):124909.
- [34] Hu YB, Li YB, Liu YQ, Li B, Christensen J. Giant elastic-wave asymmetry in a linear passive circulator. Nat Commun 2025;16:3991.
- [35] Zou XY, Liang B, Yuan Y, Zhu XF, Cheng JC. Controllable acoustic rectification in one-dimensional piezoelectric composite plates. J Appl Phys 2013;114(16): 164504.
- [36] Zhu J, Zhu XF, Yin XB, Wang Y, Zhang X. Unidirectional extraordinary sound transmission with mode-selective resonant materials. Phys Rev Appl 2020;13(4): 041001
- [37] Jin YB, Wang W, Djafari-Rouhani B. Asymmetric topological state in an elastic beam based on symmetry principle. Int J Mech Sci 2020;186:105897.
- [38] Xu GG, Li XS, Ma TX, Liu XX, Sun XW, Wang YS. Customizing acoustic and electromagnetic unidirectional states in phoxonic topological insulators. Int J Mech Sci 2025;290:110088.
- [39] Poggetto VFD, Pal RK, Pugno NM, Miniaci M. Topological bound modes in phononic lattices with nonlocal interactions. Int J Mech Sci 2024;281:109503.
- [40] An SW, Liu T, Chen YF, Li Cheng, Zhu J. Routing edge states in an anisotropic elastic topological insulator. Phy Rev Appl 2022;18:054071.
- [41] Doppler J, Mailybaev AA, Böhm J, Kuhl U, Girschik A, Libisch F, Milburn TJ, Pabl P, Noiseyev N, Rotter S. Dynamically encircling an exceptional point for asymmetric mode switching. Nature 2016;537:76–9.
- [42] Wang X, Fang XS, Mao DX, Jing Y, Li Y. Extremely asymmetrical acoustic metasurface mirror at the exceptional point. Phys Rev Lett 2019;123:214302.
- [43] JY LU, Deng WY, Huang XQ, Ke MZ, Liu ZY. Non-Hermitian topological phononic metamaterials. Adv Mater 2023:2307998.
- [44] Li XF, Ni X, Feng L, Lu MH, He C, Chen YF. Tunable unidirectional sound propagation through a sonic-crystal-based acoustic diode. Phys Rev Lett 2011;106 (8):084301.
- [45] Yuan B, Liang B, Tao JC, Zou XY, Cheng JC. Broadband directional acoustic waveguide with high efficiency. Appl Phys Lett 2012;101(4):043503.
- [46] Huang YL, Sun HX, Xia JP, Yuan SQ, Ding XL. Multi-band asymmetric acoustic transmission in a bended waveguide with multiple mechanisms. Appl Phys Lett 2016;109(1):013501.
- [47] Chen YF, Meng F, Sun GY, Li GY, Huang XD. Topological design of phononic crystals for unidirectional acoustic transmission. J Sound Vib 2017;410:103–23.
- [48] Cicek A, Adem Kaya O, Ulug B. Refraction-type sonic crystal junction diode. Appl Phys Lett 2012;100(11):111905.
- [49] An SW, Liu T, Fan HY, Gao H, Gu ZM, Liang SJ, Huang SB, Yi Zheng, Chen YF, Cheng L, Zhu J. Second-order elastic topological insulator with valley-selective corner states. Int J Mech Sci 2022;224:107339.
- [50] Chen YF, Wen XY, Lan ZH, Gu ZM, Zhu J, Su ZQ. Design of second-order phoxonic topological insulators with customized bandgaps. Int J Mech Sci 2024;274:109329.
- [51] Zhang G, Yan W, Gao YW. Higher-order elastic topological insulators with reconfigurable route and tunable corner states. Int J Mech Sci 2024;264:108820.
- [52] Al Ba'ba'a HB, Willey CL, Chen WW, Juhl AT. Theory of truncation resonances in continuum rod-based phononic crystals with generally asymmetric unit cells. Adv Theory Simul 2023;6:2200700.
- [53] Rosa MIN, Davis BL, Liu L, Ruzzene M, Hussein MI. Material vs. structure: topological origins of band-gap truncation resonances in periodic structures. Phys Rev Mater 2023;7:124201.
- [54] Park S, Yan RF, Matlack KH. Characteristics of truncation resonances in periodic bilayer rods and beams with symmetric and asymmetric unit cells. J Acoust Soc Am 2024;155:791–802.
- [55] Bastawrous M, Hussein MI. Closed-form existence conditions for bandgap resonances in a finite periodic chain under general boundary conditions. J Acoust Soc Am 2022;151:286–98.
- [56] Han B, Ji HL, Cheng L, Huang W, Qiu JH. Attenuation band splitting in a finite plate strip with two-dimensional acoustic black holes. J Sound Vib 2023;546: 117442.
- [57] Wallis RF. Effect of free ends on the vibration frequencies of one-dimensional lattices. Phys Rev 1957;105:540.
- [58] Fang X, Chuang KC, Yuan ZW, Huang ZL. Defect mode-induced unidirectional flexural wave transmission using prismatic beams with concentrated gradient masses. J Appl Phys 2018;123(22):224901.
- [59] Chen YY, Zhu R, Barnhart MV, Huang GL. Enhanced flexural wave sensing by adaptive gradient-index metamaterials. Sci Rep 2016;6(1):35048.
- [60] Chen YJ, Huang Y, Lü CF, Chen WQ. A two-way unidirectional narrow-band acoustic filter realized by a graded phononic crystal. J Appl Mech 2017;84(9): 091003
- [61] Fang T. Anti-resonances in multi-degree-of-freedom systems. Chin J Theor Appl Mech 1979;4:360–6. in Chinese.
- [62] Krylov VV, Tilman FJBS. Acoustic 'black holes' for flexural waves as effective vibration dampers. J Sound Vib 2004;274(3–5):605–19.
- [63] Pelat A, Gautier F, Conlon SC, Semperlotti F. The acoustic black hole: a review of theory and applications. J Sound Vib 2020;476:115316.
- 64] Sheng H, He MX. Ding Q. Vibration control and multifunctional design based the acoustic black hole structure: a state-of-the-art review. Int J Dyn Control 2025;13 (1):95
- [65] Deng J, Gao NS. Broadband vibroacoustic reduction for a circular beam coupled with a curved acoustic black hole via nullspace method. Int J Mech Sci 2022;233: 107641.
- [66] Zhang S, Ding LZ, Wu XW, Ma YB, Deng ZC. Vibroacoustic suppression of sandwich plates with imperfect acoustic black hole. Int J Mech Sci 2024;283:109690.

- [67] Zhu RZ, Liu YF, Bojja N, Qin ZY, Chu FL. Vibration attenuation of rotating disks via acoustic black holes. Int J Mech Sci 2023;242:108025.
- [68] Tang LL, Cheng L, Ji HL, Qiu JH. Characterization of acoustic black hole effect using a one-dimensional fully-coupled and wavelet-decomposed semi-analytical model. J Sound Vib 2016;374:172–84.
- [69] Tang LL, Cheng L. Broadband locally resonant band gaps in periodic beam structures with embedded acoustic black holes. J Appl Phys 2017;121(19):194901.
- [70] Tang LL, Cheng L. Ultrawide band gaps in beams with double-leaf acoustic black hole indentations. J Acoust Soc Am 2017;142(5):2802–7.
- [71] Bao Y, Yao ZC, Zhang Y, Hu XM, Liu XD, Shan YC, He T. Ultra-broadband gaps of a triple-gradient phononic acoustic black hole beam. Int J Mech Sci 2024;265: 108888
- [72] Deng J, Ma JF, Chen X, Yang Y, Gao NS, Liu J. Vibration damping by periodic additive acoustic black holes. J Sound Vib 2024;574:118235.
- [73] Park S, Jeon W. Ultra-wide low-frequency band gap in a tapered phononic beam. J Sound Vib 2021;499:115977.
- [74] Deng J, Gao NS, Chen X. Ultrawide attenuation bands in gradient metabeams with acoustic black hole pillars. Thin-Walled Struct 2023;184:110459.
- [75] Yao BW, Zhang YN, Zhou QB, He B, Wang GP, Rui XT. Vibration isolator using graded reinforced double-leaf acoustic black holes - theory and experiment. J Sound Vib 2024;570:118003.

- [76] Gao W, Qin Z, Chu F. Broadband vibration suppression of rainbow metamaterials with acoustic black hole. Int J Mech Sci 2022;228:107485.
- [77] Zhang YN, Chen KA, Cheng Y, Wei ZY. Lightweight-high-stiffness vibration insulator with ultra-broad band using graded double-leaf acoustic black holes. Appl Phys Express 2020;13(1):017007.
- [78] Tang LL, Cheng L. Periodic plates with tunneled acoustic-black-holes for directional band gap generation. Mech Syst Signal Process 2019;133:106257.
- [79] Tang LL, Cheng L, Chen KA. Complete sub-wavelength flexural wave band gaps in plates with periodic acoustic black holes. J Sound Vib 2021;502:116102.
- [80] Tang LL, Gao NS, Xu JL, Chen KA, Cheng L. A light-weight periodic plate with embedded acoustic black holes and bandgaps for broadband sound radiation reduction. J Acoust Soc Am 2021;150(5):3532–43.
- [81] Deng J, Chen X, Yang Y, Qin ZY, Guo WJ. Periodic additive acoustic black holes to absorb vibrations from plates. Int J Mech Sci 2024;267:108990.
- [82] Deng J, Zheng L, Gao NS. Broad band gaps for flexural wave manipulation in plates with embedded periodic strip acoustic black holes. Int J Solids Struct 2021;224: 111043.
- [83] Sheng H, He MX, Ding Q. Vibration suppression by mistuning acoustic black hole dynamic vibration absorbers. J Sound Vib 2023;542:117370.